Mapping Endothelial-Macrophage Interactions in Diabetic Vasculature: Role of TREM2 in Vascular Inflammation and Ischemic Response

Naseeb Kaur Malhi[1], Yingjun Luo[1], Xiaofang Tang[1], Rahuljeet Singh Chadha[2], Alonso Tapia[1,3], Xuejing Liu[1], Muxi Chen[1,3], Dongqiang Yuan[1], Meirigeng Qi[1,5], Lu Wei[2], John P. Cooke[4], Rama Natarajan[1,3], Kevin W. Southerland[6], Zhen Bouman Chen[1,3*]

[1]Department of Diabetes Complications and Metabolism, Arthur Riggs Diabetes and Metabolism Research Institute, City of Hope, Duarte, California, USA.

[2]Division of Chemistry and Chemical Engineering, California Institute of Technology, Pasadena, California, 91125 United States.

[3]Irell and Manella Graduate School of Biological Sciences, City of Hope, United States.

[4]Department of Cardiovascular Sciences, Houston Methodist Research Institute, Houston, Texas, USA

[5]Department of Translational Research and Cellular Therapeutics, Beckman Research Institute, City of Hope, Duarte, California, United States of America

[6]Division of Vascular and Endovascular Surgery, Department of Surgery, Duke University Medical Center, Durham, NC, 27710, USA

Correspondence addressed to Zhen Bouman Chen (zhenchen@coh.org), Department of Diabetes Complications and Metabolism, Arthur Riggs Diabetes and Metabolism Research Institute, City of Hope, Duarte, California, USA.

Abstract

Vasculopathies occur 15 years earlier in individuals with diabetes mellitus (DM) as compared to those without, but the underlying mechanisms driving diabetic vasculopathy remain incompletely understood. Endothelial cells (ECs) and macrophages (MΦ) are critical players in vascular wall and their crosstalk is crucial in diabetic vasculopathy. In diabetes, EC activation enables monocyte recruitment, which transmigrate into the intima and differentiate into macrophages (MΦ). Beyond this established model of diapedesis, EC-MΦ interplay is highly intricate and heterogenous. To capture these highly context dependent EC-MΦ interactions, we leveraged single-cell (sc)RNA-seq in conjunction with spatial transcriptome (ST)-seq profiling to analyze human mesenteric arteries from non-diabetic (ND) and type 2 diabetic (T2D) donors. We provide in this study a transcriptomic map encompassing major arterial vascular cells, e.g., EC, mononuclear phagocyte (MP), and T cells, and their interactions associated with human T2D. Furthermore, we identified Triggering Receptor Expressed on Myeloid Cells 2 (*TREM2)* as a top T2D-induced gene in MP, with concomitant increase of TREM2 ligands in ECs. TREM2 induction was confirmed in mouse models of T2D and monocyte/MΦ subjected to DM-mimicking stimuli. Perturbing TREM2 with either an antibody or silencing RNA in MPs led to decreased pro-inflammatory responses in MPs and ECs and increased EC migration *in vitro*. In a mouse model of diabetes, TREM2 expression and its interaction with ECs are increased in the ischemic, as compared to non-ischemic muscles. Importantly, neutralization of TREM2 using a neutralizing antibody enhanced ischemic recovery and flow reperfusion in the diabetic mice, suggesting a role of TREM2 in promoting diabetic PAD. Finally, we verified that both TREM2 expression and the TREM2-EC-interaction are increased in human patients with DM-PAD. Collectively, our study presents the first atlas of human diabetic vessels with a focus on EC-MP interactions. Exemplified by TREM2, our study provides valuable insights into EC-MΦ interactions, key processes contributing to diabetic vasculopathies and the potential of targeting these interactions for therapeutic development.

Introduction

Diabetes mellitus (DM) is a major global epidemic currently affecting over half a billion adults worldwide creating a substantial healthcare burden (1). DM predisposes and accelerates various vasculopathies including but not limited to coronary and peripheral arterial diseases (PAD). PAD affecting perfusion to the lower limbs is almost three times more prevalent in individuals with DM and is more likely to progress to critical limb-threatening ischemia (CLTI) (2). While it is well known that DM can cause chronic inflammation and prolonged tissue injury (3-5), the mechanisms underlying DM-induced vascular dysfunction, i.e., diabetic vasculopathy remain incompletely understood, which hampers the development of effective therapeutics for managing diabetic vasculopathy.

As with any given disease, diabetic vasculopathy involves a multitude of cell types and complex cellular communications and interactions. One of the earliest pathogenic events to occur in DM is endotheliopathy, i.e., the dysfunction of endothelial cells (ECs) lining the vascular lumen. Apart from the well-recognized role of EC dysfunction (ECD) as both a result of DM and a driver of diabetic vasculopathy, recent studies have also highlighted ECD in the development of metabolic dysfunction and DM per se (6, 7). While quiescent ECs express low levels of adhesion molecules (e.g., VCAM1, ICAM1, and MCP1) to prevent interaction with leukocytes, the diabetic milieu (e.g., hyperglycemia and elevated TNF-α levels) causes ECs to become more adhesive, enabling them to recruit monocytes, which adhere and transmigrate into the subendothelial layer and differentiate into macrophages (MΦs). The differentiated MΦs can further propagate the inflammatory response and vascular dysfunction (3).

While this classical 'diapedesis' and disease progression involving ECs and monocytes/MΦs (herein termed mononuclear phagocytes, MPs) in diabetic vasculopathy has been well established, the EC-MP interactions have mostly been studied in a unidirectional fashion. New insights have been obtained to unravel the bi-directional communications between ECs and MPs. For example, patrolling ('non-classical') monocytes crawl along the luminal space and facilitate EC homeostasis (8, 9). Within the vasculature, intimal resident MΦ are essential for maintaining a non-thrombogenic endothelial state (10, 11). Under hypoxia or ischemia, MΦ can modulate angiogenesis and collateral arterial remodeling, possibly through VEGF and MCP-1 signalings (12-14). In the development of cancer, activated MΦ can secrete inflammatory mediators to disrupt EC tight junctions and increase EC permeability (15). Furthermore, recent studies leveraging single-cell (sc) technologies have revealed unexpected heterogeneity of MΦ (16-19), with various MΦ subtypes associated with context-dependent tissue-damaging or -reparative properties. For example, both 'damaging' non-foamy inflammatory MΦ and 'reparative' fibrin-clearing aortic intima resident MΦ (Mac^{AIR}) have been identified in the intima of mouse arteries with atherosclerotic lesions (10, 20). Given the intricate EC-MP interactions and the diversity of MΦ subtypes, it is conceivable that EC-MΦ interactions are also heterogeneous, mediated by numerous and yet-to-be-defined ligand-receptor interactions, leading to differential functional consequences.

In this study, we focused on DM-induced vascular alterations, aiming to identify key EC-MΦ interactions contributing to diabetic vasculopathies. We began with single cell and spatial transcriptome profiling of human mesenteric arteries from non-diabetic donors (ND) and donors with type 2 DM (T2D) and mapped the DM-associated EC-MΦ interactions in the arterial wall. Through unbiased analyses, we identified Triggering Receptor Expressed on Myeloid Cells 2 (TREM2), a phagocytic and promiscuous receptor, to be highly upregulated in MPs in diabetic human arteries, concomitant with its interaction with dysfunctional ECs in DM. The DM-induced increase of TREM2 in MPs was validated by *in vitro* and mouse models of DM. Importantly, we identified a novel role of TREM2 in promoting DM-induced vascular inflammation and impairing EC wound-healing capacities. In a DM mouse model of hindlimb ischemia (HLI), blocking of TREM2 using a neutralizing antibody (TREM2-Ab) promoted the ischemic

recovery and flow perfusion, suggesting a disease promoting role of TREM2 in diabetic peripheral artery disease (DM-PAD). In human PAD, concomitant DM was associated with greater expression of TREM2, with a further increase in ischemic tissue compared to patient-matched non-ischemic tissue. Furthermore, we observed co-localization of TREM2 with ECs. Collectively, our study presents the first atlas of human diabetic vessels with a focus on EC-MP interactions. Exemplified by TREM2-EC interactions, our study provides valuable insights into EC dysfunction and EC-MΦ interactions, key processes contributing to diabetic vasculopathies.

Results

Profiling the diabetic transcriptome in human mesenteric intima

We began by profiling the DM-associated transcriptomic changes in vascular cells, through scRNA-seq of human mesenteric arteries from deceased organ donors with or without DM (5 ND and 4 DM) collected between 2019 and 2024, a tissue source we have described before (21-26) (**Fig. 1A, sFig. 1A**). The reasons for using mesenteric arteries include tissue availability and the demonstrated utility of using these vessels to study DM-induced vascular dysfunction (27-29). The selection of donors with DM was based upon the American Diabetes Association criteria, i.e., with a glycated hemoglobin (Hb)A1c value at 6.5% or higher. The 5 ND donors included 1 Hispanic and 4 Caucasians, all men. The 4 T2D donors included 3 Hispanic (1 woman and 2 men) and 1 Caucasian man, all obese (BMI≥30). Of note, all three Hispanic donors were untreated for their T2D, and the one Caucasian donor was noncompliant with treatment.

Based on the existing literature reporting scRNA-seq of whole blood vessels, ECs represent only 5-15% of the entire population (30-34). To enrich ECs and capture the EC-interacting cells (esp. MΦ), we scraped the inner layer of the arterial wall (including intima), using an intima scRNA-seq protocol we have established (22) (**Fig. 1B**). From 9 donors, we retrieved 14,245 cells in total, all of which passed quality control. Principal component analysis (PCA) of the batch-corrected intima scRNA-seq data revealed slight separation between ND and T2D, implying the cell populations obtained from ND and T2D donors were similar (**Fig. 1C**). Based on unsupervised clustering, these cells were separated into 17 clusters. We chose to use unbiased, default methods of analyses, to reduce the possibility of over-interpretation of our scRNA-seq data. As a result, monocytes (if present, would be differentiating) and MΦ are not distinguished, and thus named collectively as mononuclear phagocytes (MPs). Annotation of all intima scRNA-seq cells using reported cell type marker genes (31, 32, 34) identified 6 major cell types as visualized on uniform manifold approximation and projection (UMAP): ECs (~30%, consisting of 2 clusters), MPs (~26%, consisting of 5 clusters), T/NK cells (~33%, consisting of 5 clusters), fibroblasts/VSMC (7%, consisting of 2 subclusters), and others (e.g., B cells, and mast cells) (**Fig. 1D-E**). This cell composition is expected because of intima scraping and EC enrichment, with exclusion of media and adventitia.

Comparing the cell composition between ND and T2D, we observed no major difference in expression of cell marker genes in most clusters (**sFig. 2, sTable. 1**). When we compared the distribution of the major cell types, while the percentage of ECs and T cells were not substantially different (33 to 29% for ECs and 26 to 34% for T cells), MPs showed the largest shift, with an increase from 16% in ND to 30% in T2D (**Fig. 1F**). As a validation, IHC also showed more intense CD68 staining in the T2D than ND mesenteric arteries (**Fig. 1G-H**). This is in line with the notion that DM induces inflammatory infiltration and macrophage accumulation in the sub-endothelial layer (35, 36).

Endothelial and macrophage diversity in the diabetic intima

We next investigated the DM-associated transcriptomic changes within individual cell types. We first focused on ECs. Two EC clusters were identified from the intima scRNA-seq, EC1 (79% of ECs) and EC2 (21%). The proportion of EC clusters did not differ significantly between ND vs T2D. Both clusters highly express genes related to chemoattraction, angiogenesis and inflammation, typical pathways related to EC function. Interestingly, while EC1 expresses higher levels of genes encoding extracellular matrix components (e.g., *COL8A1*, *ELN*), EC2 expresses higher levels of genes related to lipid metabolism, e.g., *FABP4* and *FABP5* (**sFig. 3**), similar to EC clusters previously described (30, 37, 38). We then analyzed DEGs by comparing T2D- vs ND-EC data using RePACT, previously applied to human pancreatic islets, to identify T2D-associated DEGs (39). RePACT is sensitive in identifying disease relevant gene signatures by considering cellular heterogeneity within the same donor/sample and ranking cells by the disease pseudostate, regardless of the donor origin. RePACT analysis of the EC population from the intima scRNA-seq data revealed a remarkable difference between the transcriptome states of ND- vs T2D-ECs (**Fig. 2A,B, sFig 4A,B**), with DEGs significantly enriched for wound healing, angiogenesis, and responses to hypoxia and oxidative stress **(sFig. 4C)**. In comparison, the default Seurat analysis did not reveal clear separation of ND and T2D ECs (**sFig. 4D**) For example, genes important for inflammatory response (e.g., *CCN2*, *SEMA6B*, and *THBS1*) and those promoting endothelial-mesenchymal transition (e.g., *HEY2*, *TGFBR3*) are induced, whereas genes crucial for angiogenesis (e.g., *RAMP2*, *KLF2*, and *NOS3*) are suppressed in T2D-ECs (**Fig. 2B**). These changes are in line with the previously reported effect of DM conditions on ECs (40), which also validates the use of these human data to investigate DM-induced vascular changes.

We analyzed in parallel the DM-associated MP transcriptome and identified 935 DM-induced DEGs, including 473 up- and 462 down-regulated (**sFig 5A,B**). The top enriched pathways include innate and adaptive immune response, inflammation, as well as angiogenesis (**sFig. 5C**). We also examined expression of marker genes used to identify known myeloid subtypes (19, 34, 41). As expected, the commonly used marker genes for monocytes (*CD14*) and MΦ (*CD68*) did not differ significantly between ND and T2D (**Fig. 2C**). There was an apparent decrease in classic monocyte markers, e.g., *S100A8*, and *VCAN* in T2D MPs, suggesting more differentiation into MΦ. While the M1-like MΦ markers, e.g., *IL1B* and *TNF*, were significantly increased, the M2-like markers, e.g., *ARG1* and *CD163*, were decreased, indicative of a more pro-inflammatory state of MΦ under DM conditions. Interestingly, the marker genes of foam cells (*FABP5* and *APOE*) and TREM2^{Hi} cells (*TREM2* itself and *SPP1* and *CD9*) (42-45), were increased in T2D MPs (**Fig. 2D**). Additionally, we identified significant changes in the T cell, NK cell and B cell transcriptome between ND and T2D (with 425, 325, 862 DEGs respectively) (**sFig. 6**). Given the focus of the current study on ECs and MΦ, we did not perform further analyses of these cells.

Next, we performed trajectory analysis using Monocle 3 to infer the cell state changes induced by DM (46), focusing on ECs and MPs. While ECs showed no obvious movement through pseudotime (**sFig. 7**), the MP population, consisting of the five clusters (hereafter named MP-C1-C5) exhibited a clear trajectory ending at MP-C3, which progressed the furthest through pseudotime (**Fig. 2E**). This analysis suggests that MP-C3 encapsulates the most advanced T2D state out of all 5 MP clusters. While MP-C1 to C4 are more present in T2D, MP-C5 is more dominant in ND samples. Comparing the contribution to the MP population in ND vs T2D, MP-C3 also demonstrated the largest percentage increase, suggesting an important role of this cluster in DM-induced vascular changes (**Fig. 2F-G**). Analyzing the DM-associated changes in the 5 clusters, MP-C3 was most enriched in genes involved in angiogenesis, hypoxia response and nitric oxide biosynthetic process, all EC-relevant pathways, and pathways regulating inflammatory response and cytokine production (**sFig. 8**).

We then sought to determine the key genes within the MP-C3 contributing to the T2D state. To this end, we identified 65 genes (46 increased and 19 decreased) that are consistently differentially expressed between ND vs T2D in all the MP population as well as in MP-C3 (**sFig. 9**). Among these genes, the top ranked is *ADAM28*, a metalloprotease with functions in cell adhesion, migration, proteolysis, and signaling (47). The second ranked gene is *TREM2*, which is a promiscuous receptor highlighted in several diseases in relation to its role in macrophages, including Alzheimer's disease, obesity, and atherosclerosis. Other notable genes include *HRH2* (Histamine Receptor H2) and *PLAU* (plasminogen activator, urokinase), to which antagonists have been developed for potential DM treatment (48, 49) (**sFig. 9**).

Increased EC-MP interactions in T2D mesenteric artery

To identify EC-MP interactions with a spatial context, we performed spatial transcriptome-seq (ST-seq) using 10X Genomics Visium platform, which captures RNA on a tissue slide through spatially-encoded barcodes embedded on a 6.5 mm x 6.5 mm area and with 4992 voxel/spots of 50 μm in diameter. We performed ST-seq on 4 mesenteric arteries (2 ND vs 2 T2D) (**Fig. 3A, sFig. 10A**). These were different donors from those used for intima scRNA-seq due to the limited tissue size. While the ND arteries showed no obvious pathologies, the DM arteries show intima-media thickening (**sFig. 10B-C**). Through the Visium workflow, we captured 2,000 UMI counts from 60,000 reads per voxel/spot and 17,000 genes per sample (**sFig. 11**).

We first anchored the ST-seq data based on histology. As expected, *VWF* (an EC marker gene) was detected in the intima, where *CD68* is also detected (**Fig. 3B**). These data indicate that the ST-seq data indeed retains the spatial features of the gene expression and captures EC and MΦ in proximity. Given the 50 μm resolution of our ST-seq, which will not provide gene expression profile at single cell levels, we deconvoluted the ST-seq data with those from the scRNA-seq. For this purpose, we performed scRNA-seq of the whole arteries, which have cellular composition matching that of ST-seq to enable efficient data integration and spatial anchoring (**sFig. 12**). Through the integrative analysis of ST- and scRNA-seq, each voxel was assigned probability scores for one of the five major cell types in the arterial wall (i.e., ECs, VSMCs, MΦs, Fibroblasts and T cells). For example, we defined voxels with probability scores greater than 20% for ECs as "EC-dominant clusters". We then took all 'EC-dominant' clusters and compared the other present cell types between ND and T2D. This provides information on other cells in proximity (i.e. within 50 μm distance) to ECs, thus encompassing potential intercellular interactions. While in the ND arteries, the probability of MΦs in the 'EC-dominant' cluster was 16%, that in the T2D arteries was 41% (**Fig. 3C**), suggesting an increase in the EC-MΦ interaction in the T2D arteries.

To validate that the increased EC-MP interactions in T2D arteries also occur in the intima and identify ligand and receptors mediating these interactions, we performed CellChat and CellPhoneDB analyses with intima scRNA-seq data. These well-established bioinformatics tools allowed us to infer cell-cell communication based on gene expression level of ligand-receptor pairs (50, 51). Our analysis revealed an overall increase in intercellular interactions in T2D as compared to ND, evidenced by both the number of interactions and the interaction strength (**sFig. 13A**). EC interactions with MPs as well as with other immune (T/NK) cells were all increased in T2D (**Fig. 3D, sFig. 13B**). Focusing on the EC-MP interactions, we identified a substantial increase in bidirectional communications, exemplified by EC-derived semaphorin, THBS1, ICAM, and CXCL pathways and MP-derived VEGF, TGFβ, VCAM, and IGF pathways (**sFig 14. A,B**).

Among the EC-MP interactions, we were particularly interested in those mediated by TREM2 because of the emerging importance of TREM2 and TREM2^{Hi}-MΦ in various diseases (42-45). Furthermore,

TREM2's function as a receptor protein implicates it as a crucial gene when examining cell-cell interactions. However, the role of TREM2 in the DM-induced vasculopathy has not been reported. Considering that *TREM2* is the top-ranked receptor in all MPs and MP-C3 regulated by T2D vs ND (**sFig. 9**), we focused on TREM2 as an example to validate the EC-MP interaction and investigate the functional importance of EC-TREM2 interactions in diabetes-associated vascular function.

Consistent with the increased *TREM2* expression in T2D MPs, the expression levels of several known TREM2 ligands, including Plexin-A1 (*PLXNA1*), *LPL*, *APOE*, *HSPD1*, and *CLU* were all markedly increased in T2D ECs (**Fig. 3E**). While no TREM2 receptor-ligand complexes were detected between ECs and MPs in ND, CLU-TREM2 and APP-TREM2 pairs were present in DM (**Fig. 3F**). In line with the scRNA-seq data, the deconvolved ST-seq data revealed that TREM2 expression was increased in not only 'MP-dominant' clusters (as expected), but also 'EC-dominant' clusters in T2D arteries (**Fig. 3G**). As a validation of EC-TREM2 MΦ interactions at the protein level, co-staining of TREM2 and CD31 showed the detection of TREM2 signal in the intima layer of human T2D but not ND vessels; more importantly it appeared in close proximity to CD31 (**Fig. 3H**). These spatially resolved data, together with the scRNA-seq data, suggest that TREM2-expressing MΦs are near and interact with ECs, especially under DM conditions.

Diabetic conditions increase TREM2 expression *in vitro* and *in vivo*

As demonstrated earlier, MP-C3, the MP cluster that is most induced in intima in the DM samples and most likely to interact with ECs. In conjunction, it shows the highest *TREM2* expression, among 5 MP clusters (**Fig. 4A-B**), suggesting that increased TREM2 expression and TREM2 MΦ-EC interactions are a potential underlying mechanism of diabetic vasculopathy. To verify that DM stimuli can increase TREM2 expression, we detected *Trem2* expression in a mouse model fed high fat high sucrose (HFHS) diet, which we have previously used to induce obesity and insulin resistance (23, 52). Consistent with the human data, *Trem2* was also increased in the aortas of HFHS-fed mice (**Fig. 4C**). In line with the *in vivo* data, TREM2 expression is also increased (at both mRNA and protein levels) in THP-1-derived human MΦs and mouse RAW 264.7 MΦs treated by high glucose and TNF-α (HT), which in part mimics DM conditions (21, 23-25) (**Fig. 4D-F**). Of note, *TREM2* was also increased during the monocyte differentiation into MΦs (**sFig. 15**), as previously reported (53).

To determine the role of TREM2 in MΦ function under DM, we inhibited *TREM2* using siRNA or a neutralizing antibody (TREM2-Ab) in THP-1 monocytes. As a result of *TREM2* knockdown (KD) (evident by decreased TREM2 mRNA and protein levels) and TREM2 blocking, the adhesion of monocytes to HT-exposed ECs was substantially decreased (**Fig. 4G-I**).

TREM2 signaling pathway has been established as a critical contributor to lipid metabolism dysregulation in various pathology (54) and, more recently, shown to regulate lipid uptake in foamy macrophages in atherosclerosis (55). To examine the effect of TREM2 inhibition in lipid uptake in the context of DM, we used stimulated Raman scattering (SRS) microscopy. This non-invasive technique allows label-free chemical mapping of biomacromolecules such as lipids and proteins in biological systems (56). Although macrophages are inherently phagocytic, previous studies have reported aberrant lipid uptake and metabolism leading to dysregulated macrophage functions and increased inflammatory response (57). In our case, SRS microscopy revealed an increased lipid-to-protein ratio in macrophages in HT as compared to NM, attendant with a morphological change to a foam cell-like phenotype. Further, inhibition of TREM2 resulted in a decrease of lipid-to-protein ratio in MΦs in HT back to baseline levels (**Fig. 4J,K**) thereby suggesting a potential role of TREM2 in lipid metabolism and phagocytosis as a surface receptor. Collectively, these data suggest that TREM2 plays a crucial role in the pro-inflammatory response of MPs under diabetic conditions.

TREM2 modulates EC function in diabetic conditions

Based on the intima scRNA-seq data from human mesenteric arteries, TREM2 is most abundant in MP-C3 (**Fig. 4B**), the cluster most enriched for genes involved in EC-relevant pathways, including angiogenesis, hypoxia response and nitric oxide biosynthetic process (**sFig. 8**). Thus, we queried whether TREM2 can reciprocally regulate EC function under DM conditions. To test this hypothesis, we treated human microvascular ECs (HMVECs) with conditioned medium (CM) from THP-1-derived MΦs with or without TREM2 KD and performed wound healing scratch assays (**Fig. 5A**). Compared to CM from NM-treated MΦs, CM from HT-treated MΦs reduced the wound closure of ECs (**Fig. 5B-D**). This inhibitory effect of HT-treated MΦ CM was nearly restored by siTREM2, with faster migration across most of the timepoints measured. Importantly, addition of HT alone to the media (NM vs HT RPMI) did not affect EC wound closure, suggesting that it is the secreted factors from HT-treated MΦs, rather than HT per se, that impaired EC migration. Furthermore, compared to ECs treated with CM from MΦ under NM, those treated with CM from MΦ under HT express higher levels of pro-inflammatory markers *VCAM1* and *ICAM1*, which was abolished if TREM2 was knocked down in MΦs (**Fig. 5E,F**). Collectively, these data suggest that in DM, MΦ can regulate ECs through TREM2 to promote inflammatory responses and inhibit wound healing capacities.

TREM2 neutralization improves ischemic perfusion recovery in DM

ECs and MΦs are both crucial players in DM-induced vascular inflammation and dysfunction. Given the demonstrated effect of TREM2 inhibition in inflammatory activation and wound healing, we chose to test the role of TREM2 in ischemic recovery in a murine model of DM. Specifically, we induced hyperglycemia using streptozotocin (STZ) in C57Bl/6 mice, followed by femoral artery ligation to induce hindlimb ischemia (HLI) (**Fig. 6A, sFig. 16A**). scRNA-seq of the limb muscles revealed that *Trem2* expression was increased in MΦ in DM as compared to ND mice, and further increased in the ligated ischemic limbs as compared to the non-ischemic controls (**Fig. 6B**). This was confirmed at the protein level (**sFig. 16B**). Moreover, we also observed a higher level of TREM2 protein and its co-localization with IB4 (EC marker) in the ischemic limb (**Fig. 6C, sFig. 16C**). We then treated these mice with a local intramuscular (i.m.) injection of TREM2-neutralizing-Ab (same as used *in vitro*) (**Fig. 6D**). Compared to mice receiving IgG control, diabetic mice receiving intramuscular (i.m.) injection of TREM2-Ab showed enhanced recovery of perfusion (**Fig. 6E-F**). This was coupled with an increase in vascular density in the ischemic muscle (**sFig. 17A**). In contrast, in ND mice, TREM2-Ab did not significantly affect the recovery rate (**sFig. 17B**).

TREM2-EC interactions in human DM-PAD

To probe whether TREM2 signaling also plays a role in human PAD, which is partially modeled by the HLI in mice, we leveraged two published PAD datasets. One is bulk RNA-seq of gastrocnemius muscle from 32 healthy controls (HC) and 19 patients with CLTI, the most severe form of PAD (58), and the other scRNA-seq of (non-)ischemic muscle sites from three PAD patients (two ND and one with T2D) undergoing endovascular procedures (59). *TREM2* was found to be increased in 1) skeletal muscle from patients with CLTI vs HC (**Fig. 6G**) and 2) skeletal muscle from DM vs ND PAD patients (**Fig. 6H**). Specifically, *TREM2* levels in the muscle from PAD patients follow this order: DM-ischemic > DM-non-ischemic > ND-ischemic > ND-non-ischemic (**Fig. 6H**), similar to the mouse DM-HLI model (**Fig. 6B**). In line with the increased *TREM2* expression in the ischemic muscle, TREM2 ligands were also increased in ECs (**Fig. 6I**). Furthermore, co-staining of TREM2 and CD31 in these human tissues revealed that TREM2 protein was increased in the ischemic site (**Fig. 6J**). More importantly, TREM2 shows higher level of proximity to ECs (stained by CD31) in the ischemic sites, as compared to the non-ischemic sites (**Fig. 6J**), evident by the higher Pearson's R value of TREM2 and CD31 signals in

the ischemic vs non-ischemic sites of the same patients (**Fig. 6K**). Taken together, these data demonstrate that TREM2 and its interaction with ECs are present and increased in human DM-PAD.

Discussion

In this study, we report two major efforts focused on EC-MP interactions in DM vasculopathies. First, combining scRNA- and ST-seq, we profiled the DM-associated changes in human artery transcriptome at a single cell level in a spatial context and inferred intercellular interactions specifically between ECs and MPs (**Fig. 1-3**). Using TREM2, the top DM-induced macrophage receptor as an example, we identified its interaction with ECs and its role in modulating MP and EC function, using cell culture, a mouse model of DM-PAD, and samples from human donors with DM and PAD (**Fig. 4-6**). Collectively, our study presents the first human diabetic vascular atlas and demonstrates a crucial role of TREM2-mediated EC-MP communication in diabetic vasculopathy, with the translational relevance highlighted by findings from human PAD samples.

EC dysfunction and EC-MP interplay constitute the early and critical events driving vascular inflammation and myriad vascular diseases. To elucidate EC-MP interactions, we employed a tissue processing method to enrich intima and its associated cells. This enabled us to obtain more in-depth information regarding EC-centered intercellular interactions. In addition to EC-MP interactions, we also captured numerous EC interactions with other vascular and immune cell types and found that in DM, EC-MP interactions as well as EC communications with NK cells, T cells, and VSMCs were increased. In contrast, EC interactions with fibroblasts and B cells were decreased (**Fig. 3D**). These findings reinforce a central role of ECs in vascular response to DM by orchestrating functions of diverse cell types and provide a valuable resource for future exploration of intercellular communications and their contribution to vascular functional changes through diabetic progression.

Based on the MP transcriptome from the intima scRNA-seq from human mesenteric arteries, we identified 5 MP clusters. MP-C3 is the cluster that is most increased in T2D. We also subset the single-cell MP transcriptome into TREM2-expressing (hereafter termed 'TREM2+') and non-expressing (namely 'TREM2-') MPs (**sFig. 18**) and compared with the marker genes of reported TREM2^{Hi} MΦ. Most, if not all the reported marker genes of TREM2^{Hi} MΦ (42-45), including those involved in lipid handling and atherosclerosis are indeed expressed at a higher level in TREM2+ than TREM2-MΦ (**sFig. 19**), suggesting similarity between our TREM2+ MP and the reported TREM2^{Hi} MΦ. However, while some of the TREM2^{Hi} MΦ marker genes (e.g., ABCA1, ABCG1, and MERTK) are increased, others (e.g. ALDOA and CD36) are decreased, despite the overall TREM2 increase in T2D. This discrepancy questions the shared identify of the TREM2+ MP identified in our data and TREM2^{Hi} MΦ characterized from different tissues (e.g., brain, liver, and atherosclerotic arteries) (42-45). Additionally, we checked for marker genes of M1/M2-like MΦs and found that most of these markers were not upregulated in TREM2+ MPs, except MRC1 and CD163 (M2-like markers) (**sFig. 20**), suggesting that TREM2+ cells are neither M1-like nor M2-like. Taken together, we opted not to focus on identifying the functional role of TREM2+ MP but the role of TREM2 per se and its interactions with ECs in this study.

TREM2, primarily expressed on the surface of myeloid cells, has been shown to play crucial roles in regulating the immune response and maintaining tissue homeostasis. The regulatory role of TREM2 in various disease settings has been as promiscuous as its biochemical nature. First identified in microglia, TREM2 has been shown to promote the clearance of cellular debris in the brain, which can be protective of neurological function (60, 61). Mutations in *TREM2* have been linked to an increased risk of neurodegenerative diseases like Alzheimer's disease (AD) and frontotemporal dementia (62, 63). However, recent studies suggest that TREM2 may play a dual role in the brain and a TREM2-dependent senescent microglial population is detrimental in AD (64). In the context of metabolic

regulation, both overexpression and KO of TREM2 have been shown to promote obesity and insulin resistance (44, 65) The role of TREM2 in the vasculature has mainly been investigated in the mouse models of atherosclerosis (42, 45, 55, 66, 67). While TREM2 deletion has been shown to increase necrotic core formation in early atherosclerosis (45, 55, 68), it has also been shown to attenuate plaque progression in mice (55), highlighting a highly context-dependent role of TREM2 (43).

Considering the complex role of TREM2 in other tissues and diseases, we performed our *in vitro* and *in vivo* experiments in both baseline and DM conditions. Specifically, we found a divergent effect of TREM2 inhibition in monocyte adhesion, which was increased under NM, but decreased under HT (not shown and **Fig. 4**). By contrast, we noted a significant improvement of ischemic recovery in DM mice receiving TREM2-Ab, whereas ND mice showed no response to TREM2-Ab treatment. These context-dependent effects of TREM2 inhibition may be explained in part by different levels of TREM2 expression. It may be that for TREM2 to exert its full effect, both its expression and activation are required, as well as the presence of interacting ECs with the cognate ligands, again emphasizing the importance of cell-cell interaction in the vascular functional regulation.

TREM2 has emerged as a promising therapeutic target across various diseases. Unsurprisingly due to its context-dependent role, both TREM2 agonists and antagonists have been developed for potential use in treating Alzheimer's disease and cancer (69, 70). The observed beneficial effect of TREM2 inhibition in the diabetic mouse model with ischemic injury, complemented by the induction of TREM2 in human DM-PAD may have important therapeutic implications. On one hand, our finding may support the rationale of inhibiting TREM2 to treat inflammatory ischemic diseases, such as DM-PAD. Given that current PAD treatment is suboptimal, TREM2 targeting may present a novel therapeutic avenue (71). On the other hand, our findings may also provide caution in the development of therapeutics aiming at promoting TREM2 function, especially in patients with existing DM.

Our studies have limitations. First, we initially profiled human mesenteric arteries, which are of different vascular beds as compared to aorta in mice and microvasculature in the limb muscles. Thus, our findings from the mesenteric arteries may not fully represent the DM-associated changes in other vascular walls. Additionally, in the donors used for our intima scRNA-seq, both HbA1c and BMI are higher in the T2D, and obesity is known to increase macrophage TREM2 expression (44, 65), some changes seen may be due to obesity. However, the fact that TREM2 is increased in cultured mouse and human MPs and in the diabetic human arteries and muscle suggests that TREM2 induction and the consequent impact on EC and vascular function may be universal in diabetic vasculopathies. Second, our ST-seq mapping began in 2019 when Visium and several other powerful spatial mapping technologies (e.g. seqFISH, slide-seq, MERFISH) became available (72-74). Given our focus on the intima, which is thin (~0.1 - 0.3 mm) with abundant deposit of collagen and elastin fibers that causes autofluorescence, it would be challenging to use fluorescent-based approaches (75). To keep our study consistent, we continued to use Visium with a resolution of 50 μm, which is larger than most of the single cells. Through integration with scRNA-seq data, we were able to infer the probability of the major cell types without a true single cell resolution. Emerging technologies with increased spatial resolution will unravel novel insights into cell-cell interactions essential for vascular health and disease. Finally, using a TREM2 neutralizing antibody, we tested the role of TREM2 *in vivo* in a mouse model of DM-PAD. While we used a local i.m. injection, we cannot exclude the possibility that the TREM2-Ab may affect the ischemic recovery through action on other cells than MPs. A genetic approach using MP-specific TREM2-KO mice, in conjunction with an HLI model that mimics better the human PAD pathology may provide further validation of the functional importance of TREM2. Future studies are clearly warranted to explore the potential of targeting TREM2 as a therapeutic avenue for DM-PAD based on this first proof-of-concept study.

Methods

Human Tissues.

Human tissue studies were conducted on deidentified specimens obtained from the Southern California Islet Cell Resource Center at City of Hope. The research consents for the use of postmortem human tissues were obtained from the donors' next of kin and ethical approval for this study was granted by the Institutional Review Board of City of Hope (#01046). T2D was identified based on diagnosis in the donors' medical records as well as the percentage of glycated hemoglobin A1c (HbA1c) of 6.5% or higher. The intimal cells were isolated from human mesenteric artery by scraping the innermost layer with TrypLE as previously described (22). For cells from whole arterial tissue, cells were obtained using a TrypLE and Liberase based digestion.

Study approval.

Animal experiments were approved by the Institutional Animal Care and Use Committees at City of Hope (#18069 & #17010) and Institutional Biosafety Committee (#16023).

Single-Cell Human Mesenteric Artery RNA-Seq Sample Preparation and Analysis.

Human mesenteric arterial cells were prepared as single-cell samples for sequencing using Drop-seq protocol with 10× Genomics Chromium 3′ expression protocol as previously described (21). Fastq files were first analyzed using Cellranger (v6.1.1), the standard pipeline provided by 10X Genomics, which aligned the raw reads to human hg38 reference transcriptome. The aligned data was then processed using the R package Seurat (v3.2.3) following published guidelines. Initially, well-established filtering steps were performed to remove genes expressed in 20% mitochondrial genes were filtered out. Next, the "sctransform" normalization strategy was used where the residuals of negative binomial regression were used to model each gene. Datasets from the nine (for intima scRNA-seq) and three (for whole vessel scRNA-seq) samples then underwent integration to enable joint dimensionality reduction and clustering without being influenced by donor condition. Cells-pairs in matched biological states between samples were identified as "anchors" and used to integrate the data. The standard pre-processing step of scaling was performed prior to principal component analysis (PCA) on all cells and top 1,000 highly variable genes using the scaled z score expression values were identified. The top 15 significant principal components (PCs) were used as an input to the uniform manifold approximation and projection (UMAP) algorithm with 0.5 resolution (Seurat default). Cell clusters were generated and annotated using the following markers based on existing literature and PanglaoDB (31, 33, 38): for VSMCs, ACTA2, MYH11, WT1, and TAGLN; for ECs, VWF, PECAM1, EGFL7, ID3, GNG11, MCAM, CLDN5, and CDH5; for macrophages, CD68, MARCH1, and CD52; for fibroblasts, LUM and DCN; for T cells, CD3D and CD3E; and for NK cells, KLRD1 and NKG7. Differential expression analysis was performed on UMI counts that had been normalized using "LogNormalize" and scaled. The Seurat default, non-parametric Wilcoxon test was used to analyze genes expressed in at least 10% of cells. The log fold-change of the average expression was thresholded at 0.25 and a pseudocount of 1 was added to the averaged expression values for differential gene expression analyses.

Monocle3

Single-cell transcriptomic pseudotime analyses were performed using monocle (v3 1.3.1). Given that gene expression within this subset was normalized, the SCTransform-normalized expression matrix and corresponding metadata were extracted from the corresponding Seurat object. Metadata and SCT counts were used to create a cell_data_set object. In order to preserve clustering structure from previous analyses, we also extracted PCA/UMAP embeddings, cluster IDs, and cell type annotations

from the processed Seurat object and inserted those into the corresponding slots of the cell_data_set object. Trajectories were then inferred using the learn_graph and order_cells functions using get_earliest_principal_node to define the root of the trajectory. Cells were then recolored on a UMAP as a reflection of pseudotime.

CellChat

Cell communication analyses were carried out using the Cellchat R package (v1.5.0). We selected the CellChat human database (Interactions considered include secreted signaling, ECM-receptor, and cell-cell contacts). First, we extracted SCTransform-normalized counts from the integrated Seurat object. We created a Cellchat object for matrices from each disease status using the createCellChat() function. We subsequently identified overexpressed genes in each condition using the identifyOverExpressedInteractions. Communication probabilities were estimated with computeCommunProb and aggregated cell communication networks calculated with the aggregateNet function. We then merged ND and T2D cellchat objects using the mergeCellChat function. Differential cell communication, particularly between EC-MP were calculated and visualized using netVisual_diffInteraction, netVisual_heatmap, netVisual_embedding, netVisual_chord_gene functions. Significantly enriched pathways were denoted as those with $p < 0.05$.

CellphoneDB

To enable a systematic analysis of cell-cell communication molecules, we applied cell communication analysis based on the CellPhoneDB, a public repository of ligands, receptors and their interactions. Membrane, secreted and peripheral proteins of the cluster of different time point was annotated. Significant mean and Cell Communication significance (p-value < 0.05) was calculated based on the interaction and the normalized cell matrix achieved by Seurat Normalization.

RePACT

Seurat objects were subset for the cell type of interest (i.e. EC or MP) followed by rescaling and normalization. Disease status (i.e. ND or T2D) annotations from donors were embedded into metadata. The tool scRNA.RePACT was used to generate pseudoindices of disease state for cells. Visualization was performed using all RePACT generated tools.

Visium

The Visium spatial gene expression analysis was conducted using the Visium spatial gene expression slide and Reagent Kit (PN-1000185 and PN-1000186, 10x Genomics). We cryosectioned tissue at 10µm thickness onto the gene expression slide, making sure not to cross the fiducial frame. We then strictly followed the user guide (Rev G) to Hemoxylin and eosin (H&E) stain tissue, extract RNA and optimized a permeabilization of 37°C for 18 minutes. The cDNA amplification was performed on a touch thermal cycler (C1000, BioRad). According to the manufacture's introduction, Visium spatial libraries were constructed using Visium spatial Library construction kit (10x Genomics, PN-1000190). The libraries were then sent for sequencing at the the Integrative Genomics Core at City of Hope. H&E staining of the corresponding sections were imaged using a Zeiss Observer II light microscope at 10x using the tilescan feature. Fastq files were aligned to images and human hg38 transcriptome using 10X Genomics pipeline SpaceRanger v1.2.0. To manually annotate regions, we used LoupeBrowser 5 to cluster via histological layers and exported the data as .csv files. Next, we used Seurat v3 to perform standard quality control steps such as filtering spots with >20% mitochondrial reads and zero counts. We normalized using SCTransform as variance in molecular counts per spot can be substantial for spatial datasets and embedded histology cluster data per slice. If more than one slice of the same donor was sequenced, we merged them together before performing standard dimensionality reduction

and clustering techniques. Separate donors could not be merged as there was a clear batch effect that could not be resolved through integration. To integrate with scRNA-seq, we appled the 'anchor'-based integration workflow same as for scRNA-seq, but here it enables the probabilistic transfer of annotations from a reference to a query set. Via integration with scRNA-seq data from whole vessel, we generated predication scores for each spot of each cluster. For visualization, we used SpatialFeaturePlot.

scRNAseq murine tissue - muscle/aorta

ECs were isolated from gastrocnemius muscles of C57Bl/6 mice with a digestion buffer containing Type I collagenase in DMEM (1 mg/ml). Sorting was done with anti-CD144-conjugated magnetic beads and MACS columns (Miltenyi Biotec). For aortas, 2 aortas were collected in 1 tube and digested with M199 medium, 2 U/mL Liberase (Roche) and 0.25 U/mL Elastase (E0127, Sigma) for 35 minutes at 37ºC. DNase 10µl (QIAGEN, 27.27 Kunitz unit's RNase-free DNase I) was added and the solution was placed back at 37ºC until with monitoring until the digestion was complete. The digestion enzymes were quenched using HBSS, and the solution passed through a 70µm strainer until single cell suspension was obtained.

Western blotting

Skeletal muscle or cells were lysed with protein extraction reagent (NP40 Cell Lysis Buffer; Thermo Fisher) in the presence of a protease inhibitor (Cat# 8340; Sigma-Aldrich) and a phosphatase inhibitor cocktail (Cat# 5870; Cell Signaling). Tissue samples (total 30 µg) along with a protein marker were loaded on an 8% SDS-PAGE gel followed by transferring onto a PVDF membrane. The membranes were blocked with 5% skim milk and were incubated with primary antibodies at 1:1000 dilution in 3% BSA overnight at 4°C. The primary antibodies used were rabbit anti-TREM2 (#702886, Fisher) and rabbit anti-tubulin (#2146S, Cell Signaling). The membranes were then incubated with anti-rabbit (#7074S, Cell Signaling) or anti-mouse (#7076S, Cell Signaling) HRP-conjugated secondary antibody at room temperature for 1 h and developed using ECL substrate (Cat# WBKLS0500, Millipore).

STZ mouse model

Streptozotocin (50 mg/kg to male, 75mg/kg to female Sigma-Aldrich, USA, S0130) was administered via intraperitoneal injection to 8-12 week-old C57Bl/6 mice after 6 - 8 h of fasting for 5 consecutive days. Blood glucose was measured after 7 days of stabilization post first injection, and mice with glucose levels ≥ 16.5 mmol/L (300 mg/dL) were considered diabetic and were used for the operation.

RNA extraction and quantitative PCR

Total RNA was extracted from cells or tissues using TRIzol reagent (Thermo Fisher Scientific). cDNAs were synthesized using PrimeScript™ RT Master Mix containing both Oligo-dT primer and random hexamer primers. qPCR was performed with Bio-Rad SYBR Green Supermix following the manufacturer's suggested protocol, using the Bio-Rad CFX Connect Real Time system. β-actin was used as the internal control in human and 36B4 in mouse samples.

Stimulated Raman Scattering (SRS) Microscopy Configuration, Ratio Image Processing, and Data Analysis.

The setup of the SRS microscopy system is the same as reported previously (76). An 80 µs pixel dwell time was used to acquire images which gave an image acquisition speed of 8.52 s/frame for a 320x320 pixel field of view (FOV) at a resolution of 0.497 µm/pixel. The wavelength of the pump beam was set to 791.3 nm and 797.3 nm for $–CH_3$ (2940 cm^{-1}) and $–CH_2$ (2845 cm^{-1}) channels, respectively. Images were analyzed and color-coded using ImageJ. For CH_2:CH_3 imaging, a mask image was generated by

adjusting the threshold followed by normalization of non-zero values to one. Subsequently, CH_2 images were divided by CH_3 images from the same cell set. The resulting ratiometric image was then multiplied with the mask image to create the final ratio (CH_2:CH_3) image. The contrast was set from 0 to 1. All experiments were repeated with at least three technical and three biological replicates. MS Excel and GraphPad Prism were used for calculations and data plotting.

Culturing of THP-1 derived Macrophages and collection of cultured medium

All cells were kept under standard cell culture conditions (humidified atmosphere, 5% CO_2, 37°C). HT condition was generated by adding D-glucose into the culture media to a final concentration of 25 mM, TNFα was added to the culture media to a final concentration of 5 ng/mL. As normal glucose/osmolarity control, mannitol was added at 20 mM to the cells cultured in medium with 5 mM glucose. PMA at 20 ng/mL was added to the culture medium to enable differentiation to macrophages. Cells were transfected with scrambled control or TREM2 siRNA (Qiagen) using Lipofectamine-RNAiMAX transfection reagent (Thermo Fisher Scientific) in Opti-MEM (Thermo Fisher Scientific) to knockdown TREM2 according to manufacturer's protocol and as published.

Scratch Assay

HMVEC/HUVEC were seeded onto 12-well plates and grown to confluence. Cell monolayers were carefully wounded with a 1000-µl pipette tip to generate a cut of ~1 mm in width. After two washing steps, cells were incubated for 24 h with relevant media and area lacking cells determined by microscopy.

Hindlimb Ischemia

HLI was performed as described previously (77) with modifications. The surgical site was shaved and treated with topical antiseptic. The left femoral artery was isolated and occluded 5–6 mm distal to the inguinal ligament by ligation with 6-0 surgical silk. The control limb on the right side underwent a sham surgery without arterial ligation. Blood perfusion was measured by laser speckle flowgraphy using a PERICAM PSI Z system (Perimed AB). The ratio of blood flow in the ischemic to non-ischemic hindlimb was calculated and expressed as the perfusion recovery rate. Intramuscular injections of TREM2-Ab (R&D systems; MAB17291) or rat IgG isotype control (R&D systems; MAB0061)

Immunofluorescence/Immunohistochemistry

Tissue

Histological examinations were mainly processed by the Solid Tumor Pathology Core at City of Hope. Skeletal muscle from mice was collected and fixed in 4% PFA. For immunofluorescent (IF) staining, antibodies against CD31, IB4 fluorescein (FL1201-.5. Vector laboratories, 1:100 dilution) and TREM2 were used as primary antibodies. As secondary antibodies, Alexa Fluor555-conjugated goat anti-rat IgG (A-11007, Invitrogen, 1:200 dilution) or Alexa Fluor 488-conjugated goat anti-rabbit IgG (A-11037, Invitrogen, 1:200 dilution) were used as appropriate. Nuclei were stained with DAPI (P36935, Invitrogen). Images were taken using a ZEISS Axio Observer or ZEISS LSM 700 confocal microscope.

Cells

Cells were seeded with an attachment factor coated coverslip and exposed to relevant conditions. Cells were fixed in 4% (vol/vol) paraformaldehyde (PFA) for 10 min, and permeabilized in 0.2% (vol/vol) Triton X-100 for 5 min. A blocking buffer [0.22-mm filtered 1% (wt/vol) BSA 0.1% (vol/vol)

Triton X-100 PBS] was used to block nonspecific binding for 2 h at room temperature. We then proceeded the same as with tissue staining.

Colocalization analysis

Pearson's R value was generated by use of ImageJ Coloc2 plug-in. In brief, background staining was subtracted from each channel of interest and the pixel intensity correlation was determined. We chose Pearson's R as the most representative output.

Statistics. Statistical analyses for data other than high-throughput sequencing were performed using GraphPad Prism. Two-group comparisons were performed using 2-sided Student's t-test and multiple-group comparisons were performed using ANOVA followed by post hoc tests as appropriate (specified in figure legends). *P* values less than 0.05 were considered statistically significant.

Data and materials availability

All data needed to evaluate the conclusions in the paper are present in the paper and/or the Supplementary Materials and all high-throughput sequencing data used in this study will be depositied on GEO upon acceptance of this manuscript.

References

1. Parker ED, Lin J, Mahoney T, Ume N, Yang G, Gabbay RA, et al. Economic Costs of Diabetes in the U.S. in 2022. *Diabetes Care.* 2024;47(1):26-43.
2. Selvin E, and Erlinger TP. Prevalence of and risk factors for peripheral arterial disease in the United States: results from the National Health and Nutrition Examination Survey, 1999-2000. *Circulation.* 2004;110(6):738-43.
3. Donath MY, and Shoelson SE. Type 2 diabetes as an inflammatory disease. *Nat Rev Immunol.* 2011;11(2):98-107.
4. Sena CM, Pereira AM, and Seica R. Endothelial dysfunction - a major mediator of diabetic vascular disease. *Biochim Biophys Acta.* 2013;1832(12):2216-31.
5. Creager MA, Luscher TF, Cosentino F, and Beckman JA. Diabetes and vascular disease: pathophysiology, clinical consequences, and medical therapy: Part I. *Circulation.* 2003;108(12):1527-32.
6. Cooke JP. Endotheliopathy of Obesity. *Circulation.* 2020;142(4):380-3.
7. Tooke JE, and Goh KL. Endotheliopathy precedes type 2 diabetes. *Diabetes Care.* 1998;21(12):2047-9.
8. Auffray C, Fogg D, Garfa M, Elain G, Join-Lambert O, Kayal S, et al. Monitoring of blood vessels and tissues by a population of monocytes with patrolling behavior. *Science.* 2007;317(5838):666-70.
9. Auffray C, Sieweke MH, and Geissmann F. Blood monocytes: development, heterogeneity, and relationship with dendritic cells. *Annu Rev Immunol.* 2009;27:669-92.
10. Hernandez GE, Ma F, Martinez G, Firozabadi NB, Salvador J, Juang LJ, et al. Aortic intimal resident macrophages are essential for maintenance of the non-thrombogenic intravascular state. *Nat Cardiovasc Res.* 2022;1(1):67-84.
11. Chakarov S, Lim HY, Tan L, Lim SY, See P, Lum J, et al. Two distinct interstitial macrophage populations coexist across tissues in specific subtissular niches. *Science.* 2019;363(6432).
12. Morrison AR, Yarovinsky TO, Young BD, Moraes F, Ross TD, Ceneri N, et al. Chemokine-coupled beta2 integrin-induced macrophage Rac2-Myosin IIA interaction regulates VEGF-A mRNA stability and arteriogenesis. *J Exp Med.* 2014;211(10):1957-68.

13. Heil M, Ziegelhoeffer T, Pipp F, Kostin S, Martin S, Clauss M, et al. Blood monocyte concentration is critical for enhancement of collateral artery growth. *Am J Physiol Heart Circ Physiol.* 2002;283(6):H2411-9.
14. Schaper J, Konig R, Franz D, and Schaper W. The endothelial surface of growing coronary collateral arteries. Intimal margination and diapedesis of monocytes. A combined SEM and TEM study. *Virchows Arch A Pathol Anat Histol.* 1976;370(3):193-205.
15. Zhang S, Xie B, Wang L, Yang H, Zhang H, Chen Y, et al. Macrophage-mediated vascular permeability via VLA4/VCAM1 pathway dictates ascites development in ovarian cancer. *J Clin Invest.* 2021;131(3).
16. Haldar M, Kohyama M, So AY, Kc W, Wu X, Briseno CG, et al. Heme-mediated SPI-C induction promotes monocyte differentiation into iron-recycling macrophages. *Cell.* 2014;156(6):1223-34.
17. Zhang H, Zhang NR, Li M, and Reilly MP. First Giant Steps Toward a Cell Atlas of Atherosclerosis. *Circ Res.* 2018;122(12):1632-4.
18. Wang Z, Wu Z, Wang H, Feng R, Wang G, Li M, et al. An immune cell atlas reveals the dynamics of human macrophage specification during prenatal development. *Cell.* 2023;186(20):4454-71 e19.
19. Fernandez DM, Rahman AH, Fernandez NF, Chudnovskiy A, Amir ED, Amadori L, et al. Single-cell immune landscape of human atherosclerotic plaques. *Nat Med.* 2019;25(10):1576-88.
20. Kim K, Shim D, Lee JS, Zaitsev K, Williams JW, Kim KW, et al. Transcriptome Analysis Reveals Nonfoamy Rather Than Foamy Plaque Macrophages Are Proinflammatory in Atherosclerotic Murine Models. *Circ Res.* 2018;123(10):1127-42.
21. Calandrelli R, Xu L, Luo Y, Wu W, Fan X, Nguyen T, et al. Stress-induced RNA-chromatin interactions promote endothelial dysfunction. *Nat Commun.* 2020;11(1):5211.
22. Malhi NK, Luo Y, Tang X, Sriram K, Calandrelli R, Zhong S, et al. Isolation and Profiling of Human Primary Mesenteric Arterial Endothelial Cells at the Transcriptome Level. *J Vis Exp.* 2022(181).
23. Tang X, Luo Y, Yuan D, Calandrelli R, Malhi NK, Sriram K, et al. Long noncoding RNA LEENE promotes angiogenesis and ischemic recovery in diabetes models. *J Clin Invest.* 2023;133(3).
24. Sriram K, Luo Y, Yuan D, Malhi NK, Tapia A, Samara VA, et al. Vascular Regulation by Super Enhancer-Derived LINC00607. *Front Cardiovasc Med.* 2022;9:881916.
25. Sriram K, Qi Z, Yuan D, Malhi NK, Liu X, Calandrelli R, et al. Regulation of nuclear transcription by mitochondrial RNA in endothelial cells. *eLife.* 2024;13:e86204.
26. Lai CH, Chen AT, Burns AB, Sriram K, Luo Y, Tang X, et al. RAMP2-AS1 Regulates Endothelial Homeostasis and Aging. *Front Cell Dev Biol.* 2021;9:635307.
27. Belmadani S, Palen DI, Gonzalez-Villalobos RA, Boulares HA, and Matrougui K. Elevated epidermal growth factor receptor phosphorylation induces resistance artery dysfunction in diabetic db/db mice. *Diabetes.* 2008;57(6):1629-37.
28. Tian XY, Wong WT, Xu A, Lu Y, Zhang Y, Wang L, et al. Uncoupling protein-2 protects endothelial function in diet-induced obese mice. *Circ Res.* 2012;110(9):1211-6.
29. Pannirselvam M, Verma S, Anderson TJ, and Triggle CR. Cellular basis of endothelial dysfunction in small mesenteric arteries from spontaneously diabetic (db/db -/-) mice: role of decreased tetrahydrobiopterin bioavailability. *Br J Pharmacol.* 2002;136(2):255-63.
30. Li Y, Ren P, Dawson A, Vasquez HG, Ageedi W, Zhang C, et al. Single-Cell Transcriptome Analysis Reveals Dynamic Cell Populations and Differential Gene Expression Patterns in Control and Aneurysmal Human Aortic Tissue. *Circulation.* 2020;142(14):1374-88.
31. Wirka RC, Wagh D, Paik DT, Pjanic M, Nguyen T, Miller CL, et al. Atheroprotective roles of smooth muscle cell phenotypic modulation and the TCF21 disease gene as revealed by single-cell analysis. *Nat Med.* 2019;25(8):1280-9.

32. Hu Z, Liu W, Hua X, Chen X, Chang Y, Hu Y, et al. Single-Cell Transcriptomic Atlas of Different Human Cardiac Arteries Identifies Cell Types Associated With Vascular Physiology. *Arterioscler Thromb Vasc Biol.* 2021;41(4):1408-27.
33. Pan H, Xue C, Auerbach BJ, Fan J, Bashore AC, Cui J, et al. Single-Cell Genomics Reveals a Novel Cell State During Smooth Muscle Cell Phenotypic Switching and Potential Therapeutic Targets for Atherosclerosis in Mouse and Human. *Circulation.* 2020;142(21):2060-75.
34. Mosquera JV, Auguste G, Wong D, Turner AW, Hodonsky CJ, Alvarez-Yela AC, et al. Integrative single-cell meta-analysis reveals disease-relevant vascular cell states and markers in human atherosclerosis. *Cell Rep.* 2023;42(11):113380.
35. Schwartz MA, Vestweber D, and Simons M. A unifying concept in vascular health and disease. *Science.* 2018;360(6386):270-1.
36. Li AC, and Glass CK. The macrophage foam cell as a target for therapeutic intervention. *Nat Med.* 2002;8(11):1235-42.
37. Geldhof V, de Rooij L, Sokol L, Amersfoort J, De Schepper M, Rohlenova K, et al. Single cell atlas identifies lipid-processing and immunomodulatory endothelial cells in healthy and malignant breast. *Nat Commun.* 2022;13(1):5511.
38. Kalluri AS, Vellarikkal SK, Edelman ER, Nguyen L, Subramanian A, Ellinor PT, et al. Single-Cell Analysis of the Normal Mouse Aorta Reveals Functionally Distinct Endothelial Cell Populations. *Circulation.* 2019;140(2):147-63.
39. Fang Z, Weng C, Li H, Tao R, Mai W, Liu X, et al. Single-Cell Heterogeneity Analysis and CRISPR Screen Identify Key beta-Cell-Specific Disease Genes. *Cell Rep.* 2019;26(11):3132-44 e7.
40. Beckman JA, Doherty SP, Feldman ZB, Banks ES, Moslehi J, Jaffe IZ, et al. Comparative Transcriptomics of Ex Vivo, Patient-Derived Endothelial Cells Reveals Novel Pathways Associated With Type 2 Diabetes Mellitus. *JACC Basic Transl Sci.* 2019;4(5):567-74.
41. Mulder K, Patel AA, Kong WT, Piot C, Halitzki E, Dunsmore G, et al. Cross-tissue single-cell landscape of human monocytes and macrophages in health and disease. *Immunity.* 2021;54(8):1883-900 e5.
42. Cochain C, Vafadarnejad E, Arampatzi P, Pelisek J, Winkels H, Ley K, et al. Single-Cell RNA-Seq Reveals the Transcriptional Landscape and Heterogeneity of Aortic Macrophages in Murine Atherosclerosis. *Circ Res.* 2018;122(12):1661-74.
43. Deczkowska A, Weiner A, and Amit I. The Physiology, Pathology, and Potential Therapeutic Applications of the TREM2 Signaling Pathway. *Cell.* 2020;181(6):1207-17.
44. Jaitin DA, Adlung L, Thaiss CA, Weiner A, Li B, Descamps H, et al. Lipid-Associated Macrophages Control Metabolic Homeostasis in a Trem2-Dependent Manner. *Cell.* 2019;178(3):686-98 e14.
45. Piollet M, Porsch F, Rizzo G, Kapser F, Schulz DJJ, Kiss MG, et al. TREM2 limits necrotic core formation during atherogenesis by controlling macrophage survival and efferocytosis. *bioRxiv.* 2023:2023.05.15.539977.
46. Cao J, Spielmann M, Qiu X, Huang X, Ibrahim DM, Hill AJ, et al. The single-cell transcriptional landscape of mammalian organogenesis. *Nature.* 2019;566(7745):496-502.
47. Herat L, Rudnicka C, Okada Y, Mochizuki S, Schlaich M, and Matthews V. The Metalloproteinase ADAM28 Promotes Metabolic Dysfunction in Mice. *Int J Mol Sci.* 2017;18(4).
48. Zdilla MJ. Metformin With Either Histamine H2-Receptor Antagonists or Proton Pump Inhibitors: A Polypharmacy Recipe for Neuropathy via Vitamin B12 Depletion. *Clin Diabetes.* 2015;33(2):90-5.
49. Coudriet GM, Stoops J, Orr AV, Bhushan B, Koral K, Lee S, et al. A Noncanonical Role for Plasminogen Activator Inhibitor Type 1 in Obesity-Induced Diabetes. *Am J Pathol.* 2019;189(7):1413-22.
50. Efremova M, Vento-Tormo M, Teichmann SA, and Vento-Tormo R. CellPhoneDB: inferring cell-cell communication from combined expression of multi-subunit ligand-receptor complexes. *Nat Protoc.* 2020;15(4):1484-506.

51. Jin S, Guerrero-Juarez CF, Zhang L, Chang I, Ramos R, Kuan CH, et al. Inference and analysis of cell-cell communication using CellChat. *Nat Commun.* 2021;12(1):1088.
52. Tang X, Miao Y, Luo Y, Sriram K, Qi Z, Lin FM, et al. Suppression of Endothelial AGO1 Promotes Adipose Tissue Browning and Improves Metabolic Dysfunction. *Circulation.* 2020;142(4):365-79.
53. Cosma NC, Eren N, Usekes B, Gerike S, Heuser I, Peters O, et al. Acute and Chronic Macrophage Differentiation Modulates TREM2 in a Personalized Alzheimer's Patient-Derived Assay. *Cell Mol Neurobiol.* 2023;43(6):3047-60.
54. Li RY, Qin Q, Yang HC, Wang YY, Mi YX, Yin YS, et al. TREM2 in the pathogenesis of AD: a lipid metabolism regulator and potential metabolic therapeutic target. *Mol Neurodegener.* 2022;17(1):40.
55. Patterson MT, Firulyova MM, Xu Y, Hillman H, Bishop C, Zhu A, et al. Trem2 promotes foamy macrophage lipid uptake and survival in atherosclerosis. *Nature Cardiovascular Research.* 2023;2(11):1015-31.
56. Chadha RS, Guerrero JA, Wei L, and Sanchez LM. Seeing is Believing: Developing Multimodal Metabolic Insights at the Molecular Level. *ACS Cent Sci.* 2024;10(4):758-74.
57. Yan J, and Horng T. Lipid Metabolism in Regulation of Macrophage Functions. *Trends Cell Biol.* 2020;30(12):979-89.
58. Ryan TE, Yamaguchi DJ, Schmidt CA, Zeczycki TN, Shaikh SR, Brophy P, et al. Extensive skeletal muscle cell mitochondriopathy distinguishes critical limb ischemia patients from claudicants. *JCI Insight.* 2018;3(21).
59. Southerland KW, Xu Y, Peters DT, Lin X, Wei X, Xiang Y, et al. Skeletal muscle regeneration failure in ischemic-damaged limbs is associated with pro-inflammatory macrophages and premature differentiation of satellite cells. *Genome Medicine.* 2023;15(1):95.
60. Keren-Shaul H, Spinrad A, Weiner A, Matcovitch-Natan O, Dvir-Szternfeld R, Ulland TK, et al. A Unique Microglia Type Associated with Restricting Development of Alzheimer's Disease. *Cell.* 2017;169(7):1276-90 e17.
61. Ulrich JD, Ulland TK, Colonna M, and Holtzman DM. Elucidating the Role of TREM2 in Alzheimer's Disease. *Neuron.* 2017;94(2):237-48.
62. Leyns CEG, Ulrich JD, Finn MB, Stewart FR, Koscal LJ, Remolina Serrano J, et al. TREM2 deficiency attenuates neuroinflammation and protects against neurodegeneration in a mouse model of tauopathy. *Proc Natl Acad Sci U S A.* 2017;114(43):11524-9.
63. Liu W, Taso O, Wang R, Bayram S, Graham AC, Garcia-Reitboeck P, et al. Trem2 promotes anti-inflammatory responses in microglia and is suppressed under pro-inflammatory conditions. *Hum Mol Genet.* 2020;29(19):3224-48.
64. Rachmian N, Medina S, Cherqui U, Akiva H, Deitch D, Edilbi D, et al. Identification of senescent, TREM2-expressing microglia in aging and Alzheimer's disease model mouse brain. *Nat Neurosci.* 2024.
65. Winn NC, Wolf EM, Garcia JN, and Hasty AH. Exon 2-mediated deletion of Trem2 does not worsen metabolic function in diet-induced obese mice. *J Physiol.* 2022;600(20):4485-501.
66. Patterson MT, Xu Y, Hillman H, Osinski V, Schrank PR, Kennedy AE, et al. Trem2 Agonist Reprograms Foamy Macrophages to Promote Atherosclerotic Plaque Stability. *bioRxiv.* 2023:2023.09.21.558810.
67. Guo X, Li B, Wen C, Zhang F, Xiang X, Nie L, et al. TREM2 promotes cholesterol uptake and foam cell formation in atherosclerosis. *Cell Mol Life Sci.* 2023;80(5):137.
68. Patterson MT, Xu Y, Hillman H, Osinski V, Schrank PR, Kennedy AE, et al. Trem2 Agonist Reprograms Foamy Macrophages to Promote Atherosclerotic Plaque Stability. *Arterioscler Thromb Vasc Biol.* 2024.
69. Binnewies M, Pollack JL, Rudolph J, Dash S, Abushawish M, Lee T, et al. Targeting TREM2 on tumor-associated macrophages enhances immunotherapy. *Cell Rep.* 2021;37(3):109844.

70. van Lengerich B, Zhan L, Xia D, Chan D, Joy D, Park JI, et al. A TREM2-activating antibody with a blood-brain barrier transport vehicle enhances microglial metabolism in Alzheimer's disease models. *Nat Neurosci.* 2023;26(3):416-29.
71. Rider P, Carmi Y, and Cohen I. Biologics for Targeting Inflammatory Cytokines, Clinical Uses, and Limitations. *Int J Cell Biol.* 2016;2016:9259646.
72. Xia C, Babcock HP, Moffitt JR, and Zhuang X. Multiplexed detection of RNA using MERFISH and branched DNA amplification. *Sci Rep.* 2019;9(1):7721.
73. Rodriques SG, Stickels RR, Goeva A, Martin CA, Murray E, Vanderburg CR, et al. Slide-seq: A scalable technology for measuring genome-wide expression at high spatial resolution. *Science.* 2019;363(6434):1463-7.
74. Eng CL, Lawson M, Zhu Q, Dries R, Koulena N, Takei Y, et al. Transcriptome-scale super-resolved imaging in tissues by RNA seqFISH. *Nature.* 2019;568(7751):235-9.
75. Sartori M, Weilbaecher D, Valderrama GL, Kubodera S, Chin RC, Berry MJ, et al. Laser-induced autofluorescence of human arteries. *Circ Res.* 1988;63(6):1053-9.
76. Qian C, Liu H, Chittur PK, Chadha RS, Yao Y, Kornfield JA, et al. Quantitative Real-Time Analysis of Living Materials by Stimulated Raman Scattering Microscopy. *Anal Chem.* 2024;96(17):6540-9.
77. Meng S, Lv J, Chanda PK, Owusu I, Chen K, and Cooke JP. Reservoir of Fibroblasts Promotes Recovery From Limb Ischemia. *Circulation.* 2020;142(17):1647-62.

Acknowledgements

The authors thank Prof. Marc K. Halushka at Cleveland Clinic for histological consultation of vascular tissues and valuable discussions and critiques and Omisha Sangani at University of California, Riverside, for technical assistance.

Funding

This work was supported by NIH grants R01HL145170 (to ZBC) and R01HL106089 (to ZBC & RN), and an American Heart Association Postdoctoral fellowship 24POST1195441 (to XL), California Institute of Regenerative Medicine grant EDU4-12772 (to AT). Research reported in this publication included work performed in the Integrative Genomics, Light Microscopy and Digital Imaging, and Pathology Cores supported by the National Cancer Institute of the NIH under award number P30CA033572.

Author contributions

Conceptualization: NKM, ZBC

Methodology: NKM, YL, XT, MQ

Investigation: NKM, YL, XT, RC, AT, XL, MC, DY

Supervision: LW, RN, KWS, ZBC

Writing-original draft: NKM, ZBC

Writing-review & editing: NKM, RC, AT, MC, LW, JPC, RN, ZBC

Figures

A

Diabetic State	Age	Sex	Ethnicity	BMI	HbA1c (%)	Medical History
ND	20	M	Hispanic	26.0	5.5	No T2D-associated co-morbidities
ND	47	M	Caucasian	26.3	5.5	No T2D-associated co-morbidities
ND	62	M	Caucasian	26.0	5.1	Hypertension and high cholesterol for 5 yrs
ND	50	M	Caucasian	38.6	5.8	Hypertension and hyperlipidemia for 1 yr
ND	59	M	Caucasian	28.0	5.4	Hypertension for unknown duration
T2D	42	F	Hispanic	40.0	9.5	Untreated T2D 25 yrs, hypertension for >10 yrs, and family history of DM
T2D	46	M	Hispanic	45.8	6.9	Untreated T2D for unknown duration, high cholesterol, and family history of DM
T2D	63	M	Hispanic	35.9	7.0	Untreated T2D for 20 yrs, hypertension and hyperlipidemia for 20 yrs, family history of DM
T2D	63	M	Caucasian	33.9	6.7	Treated T2D for 10 yrs but non-compliant, hypertension for 10 yrs, and family history of DM

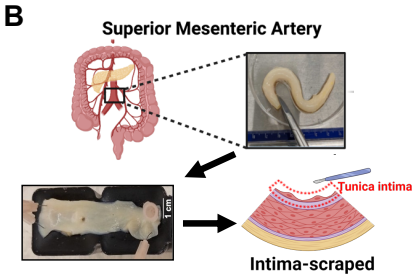

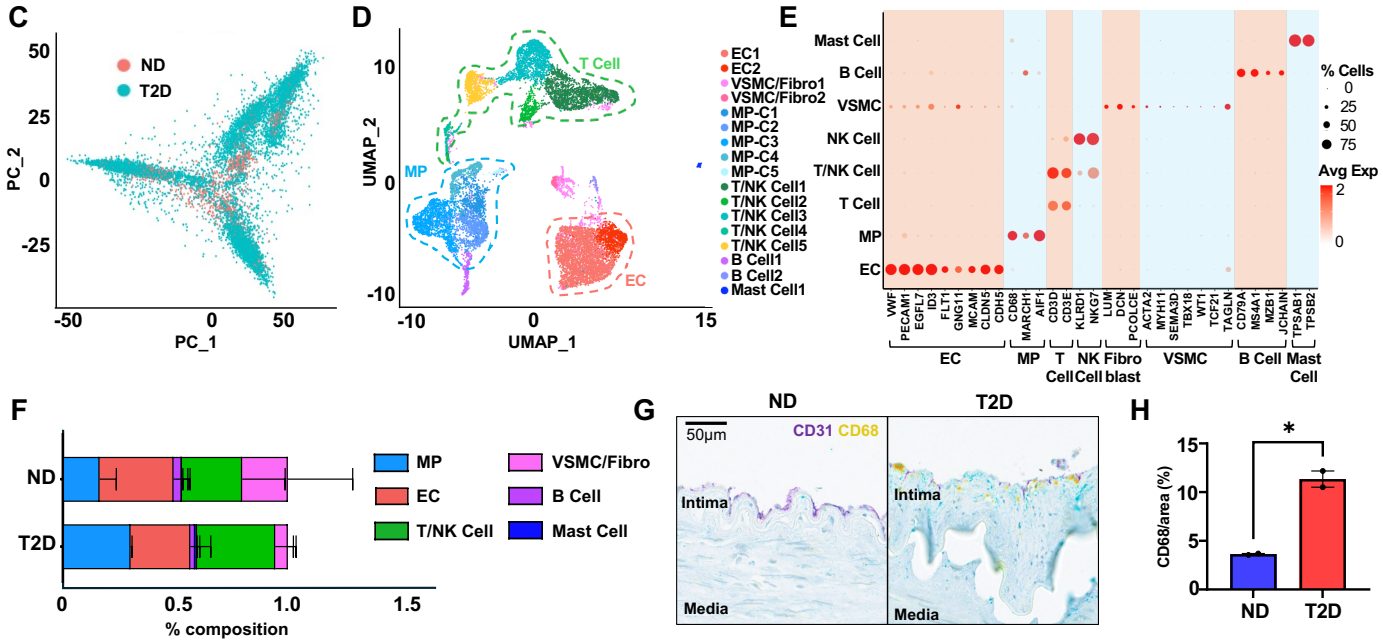

Figure 1. Profiling the diabetic transcriptome in human mesenteric intima. (A) Information of human donors of the intima scRNA-seq. ND: Non-diabetic; T2D: Type 2 diabetic. **(B)** Schematic of human mesenteric artery processing for scRNA-seq. **(C)** Principal component analysis (PCA) plot of intima scRNA-seq data, sorted by diabetic state. **(D)** Uniform manifold approximation and projection (UMAP) of scRNA-seq data, classified by 8 major cell types and subclusters generated through Seurat. EC: endothelial cell; VSMC: vascular smooth muscle cell; MP: mononuclear phagocyte; NK: natural killer. **(E)** Dotplot showing levels of cell-marker genes (x axis) within each annotated cell population (y axis). **(F)** Cell composition (%) of the intima scRNA-seq data from ND vs T2D donors. **(G,H)** Representative CD31 and CD68 staining and CD68 quantification of mesenteric arteries (3 ND and 2 T2D), expressed as percentage of analyzed tissue area. Bar graphs represent mean ± SEM.

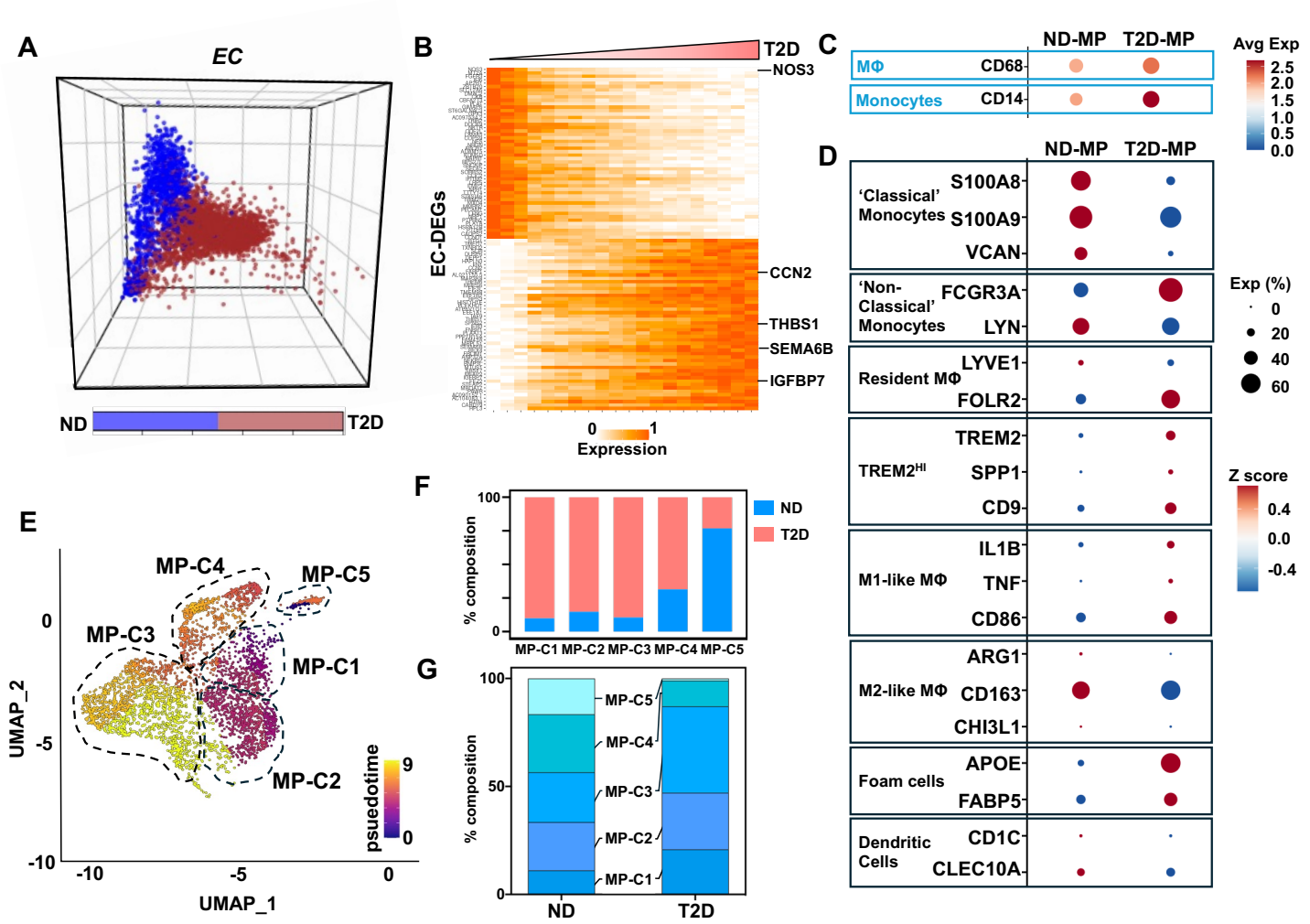

Figure 2. DM-induced transcriptome shifts in EC and MP. (A) All ECs are plotted in the 3D space of the top 3 principal components. Cells were colored based on the donor's DM state. **(B)** Heatmap demonstrating the 50 top and bottom T2D trajectory genes. Each row represents the expression of a DEG in single cells ranked by the pseudo-T2D state. **(C)** Gene expression of CD68 (macrophage marker) and CD14 (monocyte marker) in MPs between ND and T2D. **(D)** Gene expression of MP subtype markers between ND and T2D, plotted with z scores. **(E)** Intima scRNA-seq MPs colored by pseudotime as calculated by Monocle3 superimposed on UMAP. Note that MP-C3 progressed furthest through pseudotime. **(F)** Contribution of ND vs T2D samples to each of the five MP clusters (MP-C1-C5). **(G)** Percentage of MP-C1-5 in total MP population from ND and T2D samples.

A

Donor ID	Diabetic State	Age	Sex	Race	BMI	HbA1c (%)	Medical history
ND-1	ND	62	M	Caucasian	26	5.1	Hypertension and hypercholesterolemia for 5 yrs
ND-2	ND	44	M	Caucasian	24.4	5.3	No T2D-associated co-morbidities
T2D-1	T2D	34	M	Hispanic	27.6	7.5	Treated T2D for 7 yrs. Hypercholesterolemia for 5 yrs
T2D-2	T2D	58	M	Hispanic	22.9	10.5	Treated T2D for 8 years. Treated hypertension for 15 yrs

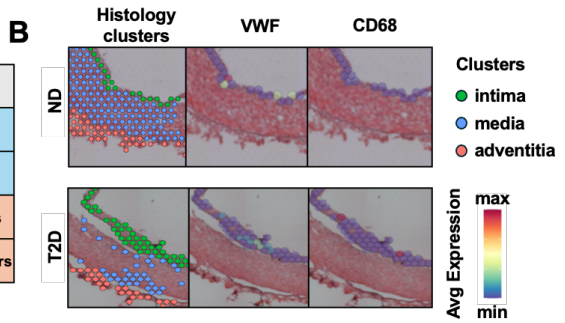

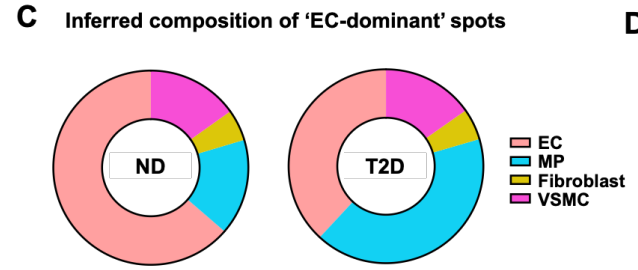

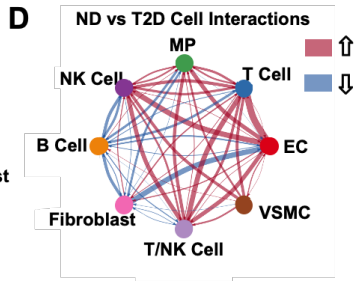

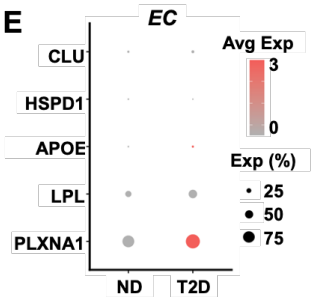

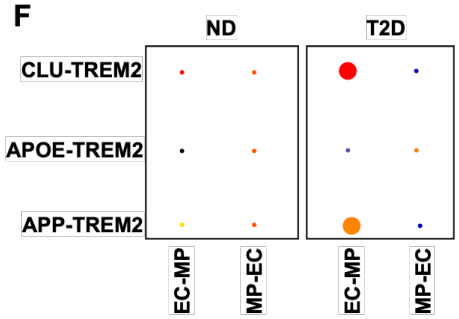

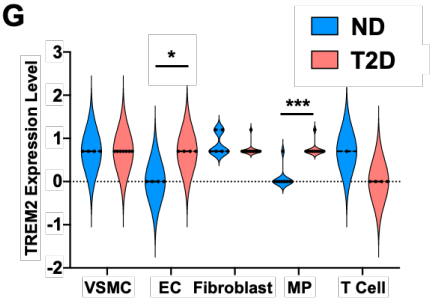

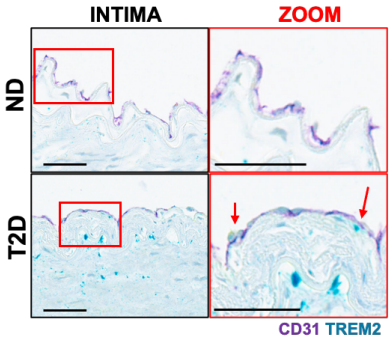

Figure 3. Increased EC-MP and EC-TREM2 interactions in T2D arteries. (A) Information of human donors included in the spatial transcriptome sequencing (ST-seq). **(B)** SpatialFeaturePlots of VWF and CD68 expression in the intima as revealed by ST-seq. Left plots show histology-guided annotation. **(C)** Pie charts showing probability of the presence of specific cell types within 'EC-dominant' spots/voxels in ND and T2D mesenteric arteries, computed through integrative analysis of ST-seq and whole-artery scRNA-seq. **(D-F)** Analysis for EC-MP interactions based on intima scRNA-seq data. **(D)** Comparison of intercellular interactions between ND vs T2D computed through CellChat. **(E)** Gene expression of TREM2 ligands in ND vs T2D ECs. **(F)** CellphoneDB analysis reveals the TREM2-ligand complexes between MPs and/or ECs in ND and T2D arteries. **(G)** TREM2 expression levels in ST-seq spots/voxels with specific dominant cell types as indicated, determined through integrative analysis of ST- and scRNA-seq. *$p<0.05$, ***$p<0.001$ based on Students t-test. **(H)** Immunohistochemistry of human mesenteric arteries for CD31 and TREM2, from left to right showing higher magnification and zoom-in images. Scale bar = 50µm.

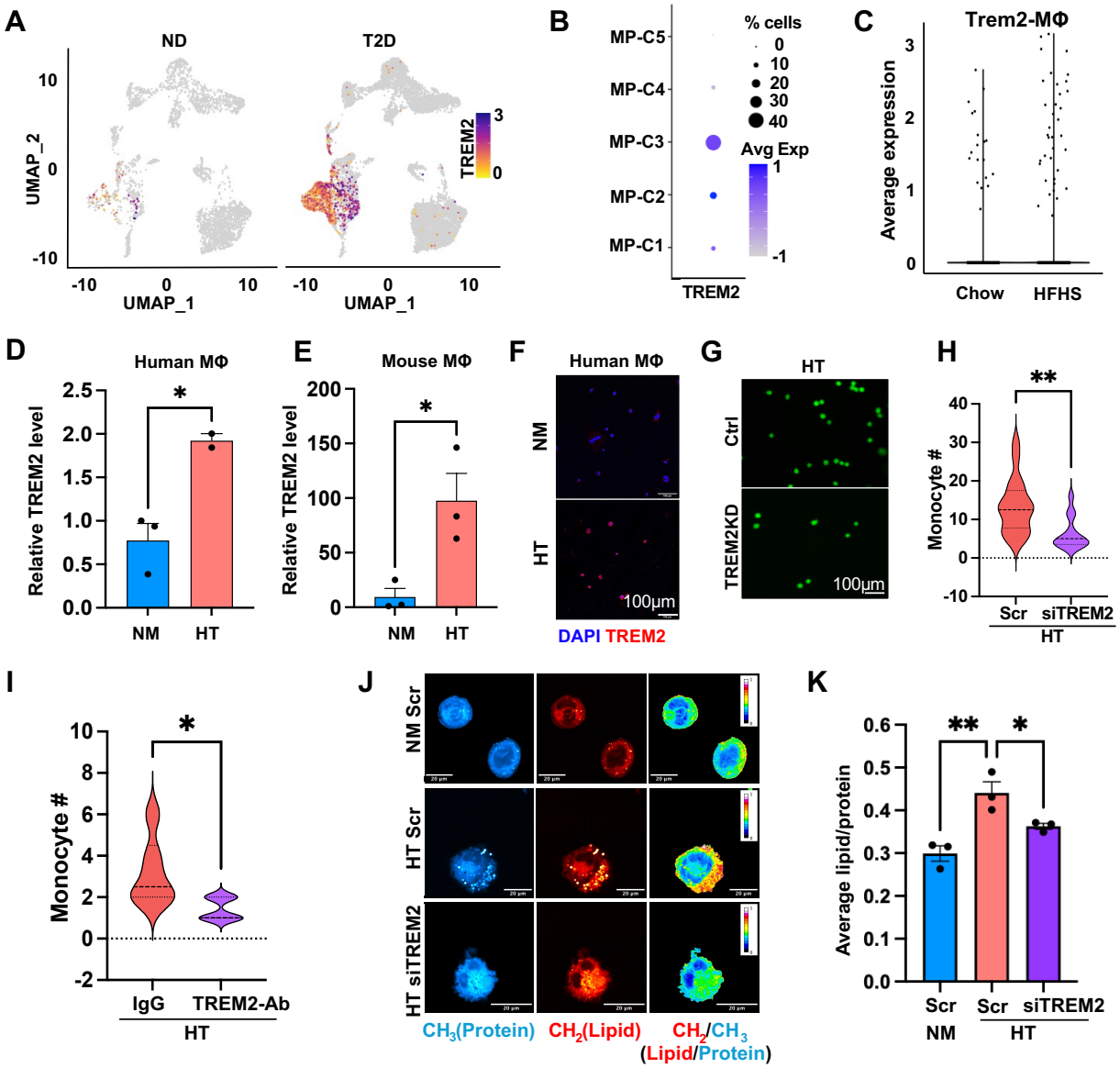

Figure 4. TREM2 expression is increased in DM-MP and promotes inflammatory activation. (A,B) TREM2 expression in ND and T2D donors (in A) and in 5 MP clusters (C1-C5) (in B) quantified by intima scRNA-seq. **(C)** Trem2 expression in the aortic MΦs from male C57Bl/6 mice fed chow vs HFHS diet for 4 months (n = 4/group), profiled by scRNA-seq. (**D,E)** Relative TREM2 mRNA levels measured by qPCR in human MΦ (THP-1 derived) (in D) and mouse MΦ (Raw 264.7) (in E) treated with 25 mM Glucose plus TNFα (HT) for 72 hr or 25mM mannitol as normal glucose osmolarity control (NM). Graphs represent mean ± SEM**. (F)** Immunofluorescence staining of TREM2 in THP-1-derived MΦs under NM and HT, with DAPI counterstain. **(G-I)** Leukocyte adhesion assay with ECs cultured under HT for 72 hr and incubated with CMFDA labeled THP-1 cells with or without TREM2 knockdown (in G, H) or neutralizing antibody against TREM2, with IgG as isotype control (in I). **(G)** Representative images and (H,I) quantification of adhered monocytes. (**J)** Representative SRS images of THP-1-derived MΦ under treatments as indicated. The first and the second column represent single-frequency SRS images targeted at the protein (–CH_3 symmetric stretching, 2940 cm^{-1}) and lipid (–CH_2 symmetric stretching, 2845 cm^{-1}) channels, respectively. The third column represents the ratiometric images of CH_2/CH_3 (lipid/protein). Scale bar = 20 μm. **(K)** Quantification of average lipid/protein ratios from (**J**), plotted with mean ± SEM from 3 independent experiments. *p<0.05, **p<0.01 based on Student's t test (in D, E, G, H) or one-way ANOVA followed by Dunnets test (in K)**.**

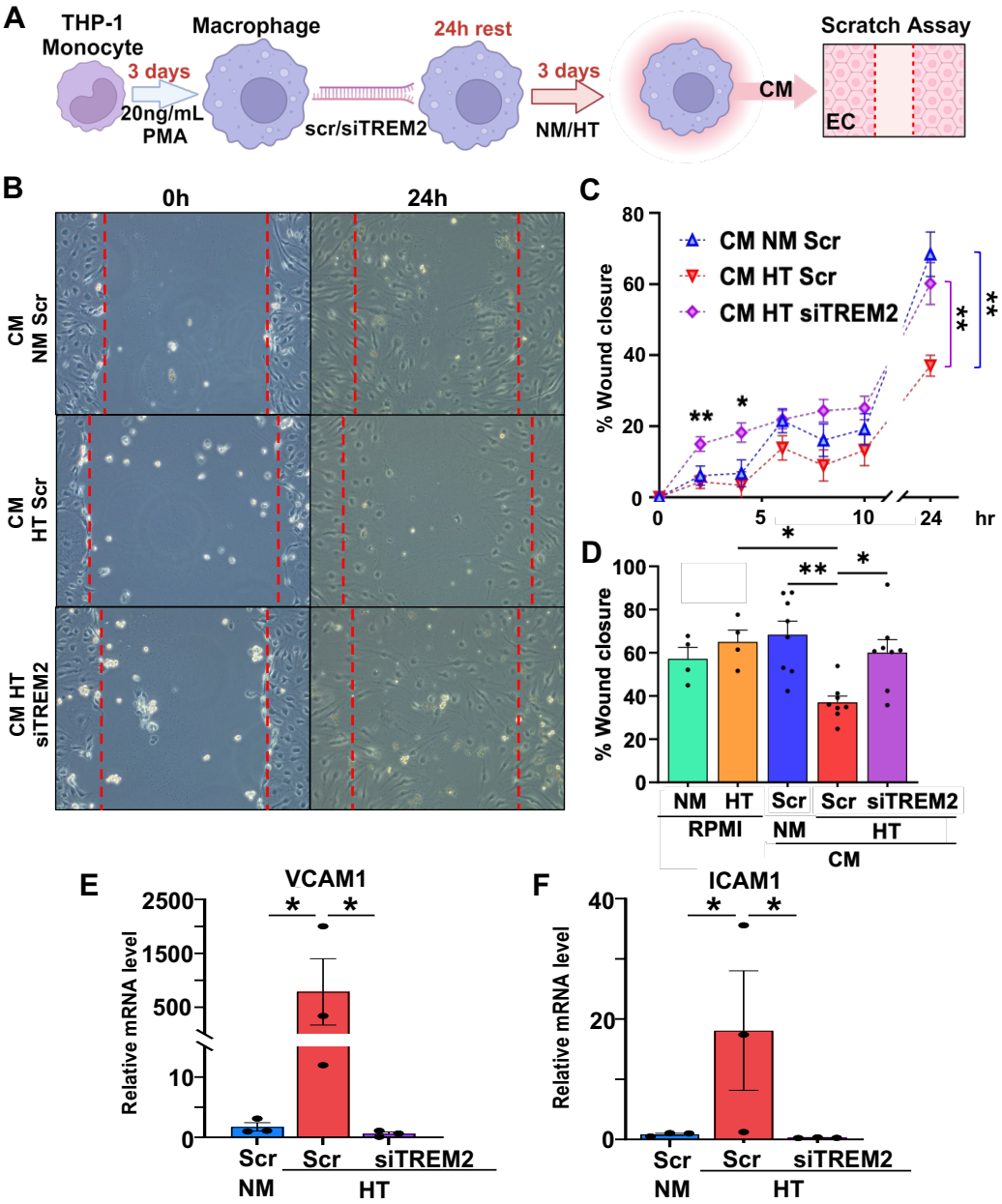

Figure 5. TREM2 modulates EC function in diabetic conditions. (A) Schematic of scratch wound assay using HMVECs and conditioned medium (CM) from THP-1-derived MΦ with or without TREM2 knockdown and treated by NM/HT. **(B,C)** Representative images and quantification of scratch wound assay using ECs incubated with MΦ CM across a 24 h time course. **(D)** Area under curve at 24 h showing the % wound closure based on (C). **(E)** qPCR of *VCAM1* and *ICAM1* expression in ECs treated with MΦ CM. Data represents mean ± SEM of n = 5 (B-D) and n = 3 (E). *p<0.05, **p<0.01 based on ANOVA followed by Dunnets post-hoc test.

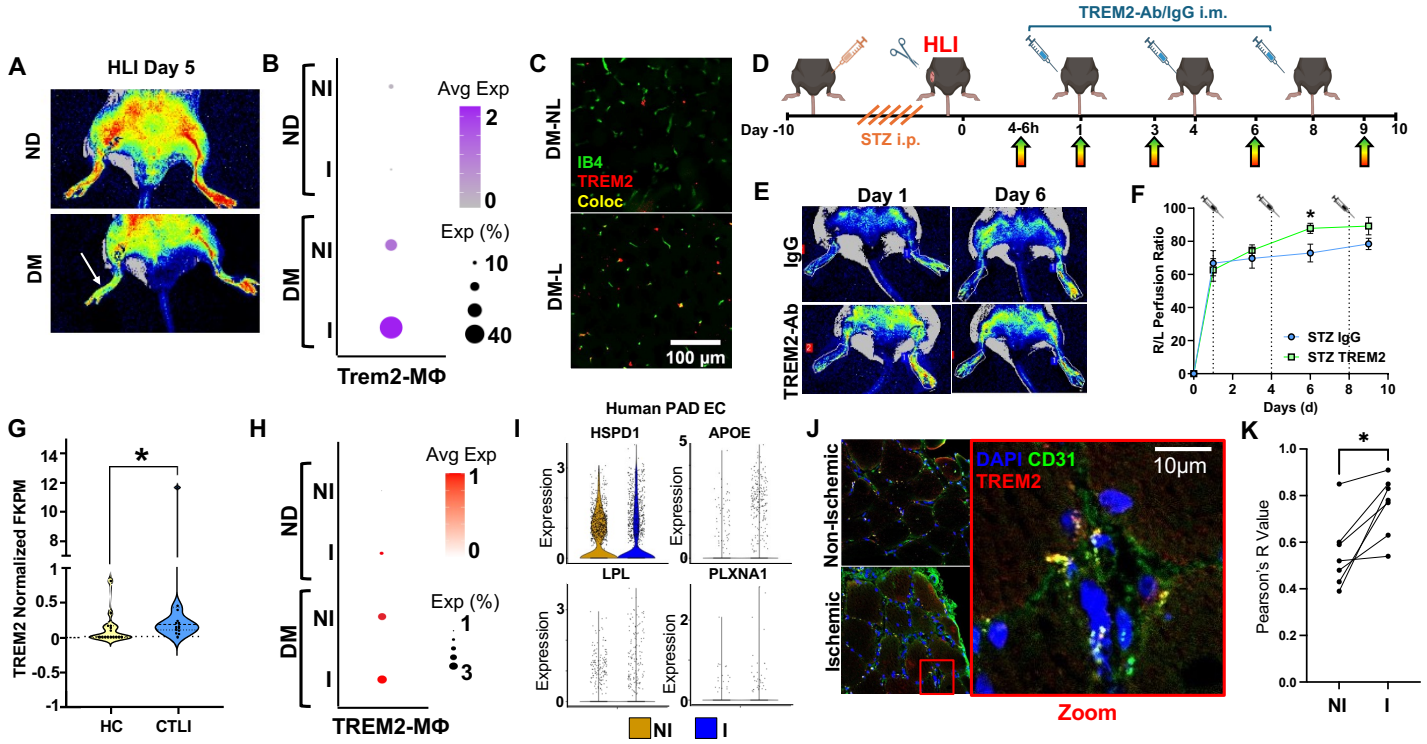

Figure 6. Induction of TREM2 in DM-PAD and its effect in ischemic recovery. **(A)** Laser speckle images of flow perfusion in male mice treated with or without STZ (DM vs ND), 5 days post hindlimb ischemia (HLI). Note the decreased flow in the ligated right limb (white arrow) of DM mouse as compared to ND. (**B)** MΦ TREM2 expression in non-ligated (NI) or ligated (I) limb muscles from ND and DM mice, as profiled by scRNA-seq (n = 2/group). **(C)** IB4-TREM2 co-IF on the non-ligated vs ligated limb muscles from DM mice. **(D-F)** DM was induced in male and female C57Bl/6 mice followed by HLI and intramuscular injection of TREM2 neutralizing antibody (TREM2-Ab) into the ischemic limbs on post-op Day 1, 4, & 8. IgG was used as an isotype control. (**E)** Representative images of flow perfusion on Day 1 and 6. **(F)** Quantification of perfusion ratio, calculated by comparing the flow perfusion in the ligated vs non-ligated (R/L) limb of the same animals. Data represented as mean ± SEM of n = 8/group (mixed between n = 7 male and n = 9 female). **(G)** TREM2 mRNA levels determined by bulk RNA-seq of from muscle biopsy of human healthy control (HC/n = 61) and patients with critical limb ischemia (CTLI/n = 64), as published (Ryan et al., 2018). **(H-J)** scRNA-seq profiled expression of *TREM2* (in H) and TREM2 ligand in ECs (in I) in the surgically collected (non-)ischemic (NI/I) muscles from human PAD patients with (n = 1) or without (n = 2) co-existing DM. **(J,K)** CD31-TREM2 co-IF in (non-)ischemic muscles from human patients with PAD (n = 7). (J) shows representative images and (K) shows quantification of CD31-TREM2 co-staining expressed by Pearson's R values. *p<0.05 based on paired t-test.